The Energy Budget of the Polar Atmosphere in MERRA

RICHARD I. CULLATHER

Earth System Science Interdisciplinary Center, University of Maryland, College Park, College Park, Maryland

MICHAEL G. BOSILOVICH

Global Modeling and Assimilation Office, NASA Goddard Space Flight Center, Greenbelt, Maryland

(Manuscript received 14 October 2010, in final form 12 June 2011)

ABSTRACT

Components of the atmospheric energy budget from the Modern-Era Retrospective Analysis for Research and Applications (MERRA) are evaluated in polar regions for the period 1979–2005 and compared with previous estimates, in situ observations, and contemporary reanalyses. Closure of the budget is reflected by the analysis increments term, which indicates an energy surplus of 11 W m^{-2} over the North Polar cap (70°–90°N) and 22 W m^{-2} over the South Polar cap (70°–90°S). Total atmospheric energy convergence from MERRA compares favorably with previous studies for northern high latitudes but exceeds the available previous estimate for the South Polar cap by 46%. Discrepancies with the Southern Hemisphere energy transport are largest in autumn and may be related to differences in topography with earlier reanalyses. For the Arctic, differences between MERRA and other sources in top of atmosphere (TOA) and surface radiative fluxes are largest in May. These differences are concurrent with the largest discrepancies between MERRA parameterized and observed surface albedo. For May, in situ observations of the upwelling shortwave flux in the Arctic are 80 W m^{-2} larger than MERRA, while the MERRA downwelling longwave flux is underestimated by 12 W m^{-2} throughout the year. Over grounded ice sheets, the annual mean net surface energy flux in MERRA is erroneously nonzero. Contemporary reanalyses from the Climate Forecast Center (CFSR) and the Interim Re-Analyses of the European Centre for Medium-Range Weather Forecasts (ERA-I) are found to have better surface parameterizations; however, these reanalyses also disagree with observed surface and TOA energy fluxes. Discrepancies among available reanalyses underscore the challenge of reproducing credible estimates of the atmospheric energy budget in polar regions.

1. Introduction

The objective of this study is to examine the performance of the Modern-Era Retrospective Analysis for Research and Applications (MERRA) in representing the high-latitude atmospheric energy budget. MERRA was recently released by the National Aeronautics and Space Administration Global Modeling and Assimilation Office (GMAO). This effort, as well as a companion paper examining the atmospheric moisture budget (Cullather and Bosilovich 2011), represent an initial examination of this reanalysis in the polar regions.

A quantitative knowledge of the flow, storage, and conversion of energy within the climate system has evolved with time as a result of contributions made by improvements in the observing system and by numerical atmospheric reanalyses (e.g., Fasullo and Trenberth 2008). In polar regions, the energy budget and its variability are frequently used as a diagnostic for understanding rapidly changing conditions including glacial mass balance and perennial sea ice reduction (e.g., Porter et al. 2010). As noted in Cullather and Bosilovich (2011), numerical reanalyses are widely used in polar research for evaluating polar processes, as boundary conditions for limited area atmosphere and ocean–sea ice models and as a first-order validation for climate models. However, reanalyses inevitably contain inaccuracies resulting from limitations in the observing system, inconsistencies between observing methods, and incomplete knowledge of the physical

Corresponding author address: Richard Cullather, % NASA/GSFC Code 610.1, 8800 Greenbelt Road, Greenbelt, MD 20771.
E-mail: richard.cullather@nasa.gov

DOI: 10.1175/2011JCLI4138.1

© 2012 American Meteorological Society

processes that are represented in the assimilating weather forecast model. In particular, surface albedo characteristics over polar oceans and high-latitude cloud properties are both associated with important but complex energy feedback mechanisms that have historically been poorly simulated (Randall et al. 1998). An initial evaluation of the high-latitude energy budget in a reanalysis record is therefore a constructive activity.

Some questions of interest pertaining to this study are as follows.

- What are the spatial and temporal patterns of energy budget components in MERRA, and how do they compare with previous studies and contemporary reanalyses?
- How do MERRA surface fluxes compare with in situ field studies?
- What is the nature of adjustment terms in the energy budget?

Section 2 provides an overview of the MERRA dataset and method. An evaluation of the atmospheric energy balance in polar regions is given in section 3. A discussion of these comparisons is then given in section 4.

2. MERRA description and method

A description of the MERRA system is given by Cullather and Bosilovich (2011) and Rienecker et al. (2011), and is summarized here. MERRA was made using the Data Assimilation System component of the Goddard Earth Observing System (GEOS DAS; Rienecker et al. 2008), and covers the modern satellite era from 1979 to the present. The assimilation system utilizes the GEOS model, version 5 (GEOS-5): a finite-volume atmospheric general circulation model (AGCM) that is used for operational numerical weather prediction. For MERRA, the GEOS DAS was run at a horizontal resolution of ⅔° longitude by ½° latitude and 72 hybrid-sigma coordinate vertical levels to produce an observational analysis at 6-h intervals. Boundary conditions include climatological aerosol and solar forcing. Sea surface temperature and sea ice are linearly interpolated in time from weekly 1° resolution Reynolds fields (Reynolds et al. 2002). The atmospheric model is coupled to a catchment-based hydrologic model on land (Koster et al. 2000) and a sophisticated multilayer snow model (Stieglitz et al. 2001) that is coupled to the catchment hydrology. Land surface albedos are derived from retrievals of the Moderate Resolution Imaging Spectroradiometer (MODIS; Moody et al. 2005). The global 30 arc-second elevation dataset (GTOPO30) produced by the Earth Resources Observation Systems (EROS) Data Center of the U.S. Geological Survey (Gesch 1994) is used in MERRA.

MERRA utilizes the incremental analysis update (IAU) assimilation method (Bloom et al. 1996). In the IAU method, an analysis increment is computed for a given variable as the difference between an initial 6-hourly observation-based analysis field and the background model state. Observations consist of in situ reports provided by the U.S. National Centers for Environmental Prediction and available satellite data. The analysis increment is expressed as a tendency. The model is then run again over the 6-h interval using this tendency as an additional forcing term. The resulting MERRA product is then composed of dynamically consistent 1-hourly fields that are incrementally corrected to observation every six hours. The sum of analysis increments quantify the adjustment terms in atmospheric balance equations. Thus atmospheric budgets—as constructed in the GEOS-5 AGCM—and their analysis increments are maintained within MERRA to the accuracy limited by round-off and data compression errors. Temporal averages provided by MERRA are computed at the model time step.

Following a form similar to Trenberth (1997), the MERRA total energy equation integrated over the atmospheric column may be written as

$$\frac{\partial A_E}{\partial t} + \nabla \cdot \tilde{\mathbf{F}}_A = R_{\text{top}} + F_{\text{sfc}} + L_v \frac{\partial W_v}{\partial t}\bigg|_{\text{CHM}} + \left[L_v \frac{\partial W_v}{\partial t} - L_f \frac{\partial W_i}{\partial t}\right]\bigg|_{\text{FIL}} + \text{ANA}_{(E)} - Q_{\text{NUM}}, \quad (1)$$

where A_E is total energy in the atmospheric column, $\tilde{\mathbf{F}}_A$ is the horizontal transport of total atmospheric energy, R_{top} is the downward net radiative flux at the top of the atmosphere (TOA), F_{sfc} is the upwelling net surface flux, L_v is the latent heat of vaporization, L_f is the latent heat of fusion, W_v is column-integrated water vapor (precipitable water), and W_i is column-integrated cloud ice condensate. The term denoted by the subscript "CHM" represents latent heat arising from a parameterized source of water vapor in the middle atmosphere from the model chemistry routine, which is small (Suarez 2011). The notation "FIL" refers to tendencies associated with the "filling" of spurious negative water (Suarez 2011), which was found to be negligible in all cases. The term $\text{ANA}_{(E)}$ is the sum of contributions to the analysis increment, which again is the difference between the observation-based analysis and the corresponding model synoptic background. The analysis increment tendency represents the summation of vertically integrated latent heat, virtual enthalpy, kinetic, and potential energy term contributions. The analysis increment associated with virtual enthalpy arises from differences between the atmospheric virtual temperature

profile of the model state and that of the observation-based analysis. The analysis increment associated with latent heat is associated with differences in the atmospheric moisture content. The kinetic energy analysis increment is associated with differences in the horizontal winds, and the potential energy analysis increment arises from differences in the surface pressure. The term Q_{NUM} denotes the contribution of spurious residuals resulting from inertial terms, the discretization of the thermodynamic equation, coordinate remapping during model integration, and time-truncation errors.

Similar to the description of the atmospheric moisture budget in Cullather and Bosilovich (2011), it may be seen that terms on the left-hand side of the energy budget in (1) are derived from state and dynamic variables in the atmospheric profile, while the first two terms on the right-hand side are output products of the assimilating model's physical parameterizations. Variables that are attributable to physical parameterizations may be seen as having a higher degree of uncertainty as compared with state and dynamical variables (e.g., Kalnay et al. 1996). Disregarding negligible chemistry and moisture filling terms, the equation is balanced by analysis increments and the spurious residual term Q_{NUM}.

The time rate of change in total atmospheric energy storage A_E is expressed as

$$\frac{\partial A_E}{\partial t} = L_v \frac{\partial W_v}{\partial t} - L_f \frac{\partial W_i}{\partial t} + \frac{\partial}{\partial t}\left[\int_{p_{\mathrm{top}}}^{p_{\mathrm{sfc}}} (c_P T_v + \Phi_S + k)\frac{dp}{g}\right], \qquad (2)$$

where p_{sfc} is surface pressure; p_{top} is the fixed pressure at the top model level, which is 0.01 hPa; c_P is the specific heat of the atmosphere at constant pressure; T_v is virtual temperature; Φ_S is surface geopotential; $k = 1/2|\tilde{\mathbf{V}}|^2$ is kinetic energy; and g is the gravity constant. The product $c_p T_v$ is referred to as virtual enthalpy. The divergence term may be expanded as follows:

$$\begin{aligned}\nabla\cdot\tilde{\mathbf{F}}_A = {} & \nabla\cdot\int_{p_{\mathrm{top}}}^{p_{\mathrm{sfc}}} (L_v q_v - L_f q_i)\tilde{\mathbf{V}}\frac{dp}{g} \\ & + \nabla\cdot\int_{p_{\mathrm{top}}}^{p_{\mathrm{sfc}}} c_P T_v \cdot \tilde{\mathbf{V}}\frac{dp}{g} + \nabla\cdot\int_{p_{\mathrm{top}}}^{p_{\mathrm{sfc}}} \Phi\cdot\tilde{\mathbf{V}}\frac{dp}{g} \\ & + \nabla\cdot\int_{p_{\mathrm{top}}}^{p_{\mathrm{sfc}}} k\cdot\tilde{\mathbf{V}}\frac{dp}{g}, \qquad (3)\end{aligned}$$

where Φ is geopotential within the atmospheric column. The net upward surface flux is given as

$$F_{\mathrm{sfc}} = Q_H + Q_E + L_f P_s - R_{\mathrm{sfc}}, \qquad (4)$$

where Q_H and Q_E are the upwelling surface turbulent sensible and latent heat fluxes, the product $L_f P_s$ is latent heating resulting from solid precipitation, and R_{sfc} is the net downward radiative flux at the surface. The relation between MERRA variables and equation notation is given in the appendix.

The approach of this study is to evaluate MERRA values against prior studies for large-scale areal averages of the terms in (1)–(4) over fixed polar regions as shown in Fig. 1, with a particular focus on the polar caps. Studies for comparison include Nakamura and Oort (1988), Genthon and Krinner (1998), Serreze et al. (2007), and Porter et al. (2010). Nakamura and Oort (1988) produced budget estimates for both polar caps using the ocean flux values of Levitus (1984), composite satellite data from the period 1966–77, and atmospheric circulation statistics from Oort (1983), which are based on the upper-air station network. Nakamura and Oort (1988) found the observational network insufficient for computing atmospheric energy transport into the South Polar cap and instead produced output from the NOAA Geophysical Fluid Dynamics Laboratory GCM. Genthon and Krinner (1998) used the 15-yr European Centre for Medium-Range Weather Forecasts Re-Analysis (ERA-15; Gibson et al. 1997) for the period 1979–93 to evaluate the South Polar cap. Serreze et al. (2007) examined the North Polar cap and Arctic Ocean domains using the more recent 40-yr Re-Analysis (ERA-40; Uppala et al. 2005) and the National Centers for Environmental Prediction–National Center for Atmospheric Research (NCEP–NCAR) Reanalyses (Kalnay et al. 1996) for the period 1979–2001. Serreze et al. also examined TOA radiative fluxes from the Earth Radiation Budget Experiment (ERBE) for the study period February 1985 to April 1989 (Barkstrom 1984). Porter et al. (2010) similarly examined the North Polar cap energy budget for the period November 2000–October 2005 using the 25-year Japanese Reanalysis (JRA-25; Onogi et al. 2007) and satellite data from the Clouds and the Earth's Radiant Energy System (CERES; Wielicki et al. 1996) product. In support of budget comparisons with these previous studies, the evaluation of near-surface state variables against in situ station observations is also instructive. The results presented here are for the years 1979–2005.

Corresponding values for surface and TOA energy fluxes are also tabulated for two contemporary reanalyses for comparison: the ECMWF Interim product (ERA-I; Simmons et al. 2007) and the NCEP Climate Forecast System Reanalysis (CFSR; Saha et al. 2010). The ERA-I was produced at T255 spectral resolution, which is similar to the grid resolution of MERRA. Energy flux fields are produced from 12-h forecasts initialized by four-dimensional variational (4DVAR) assimilation. Monthly

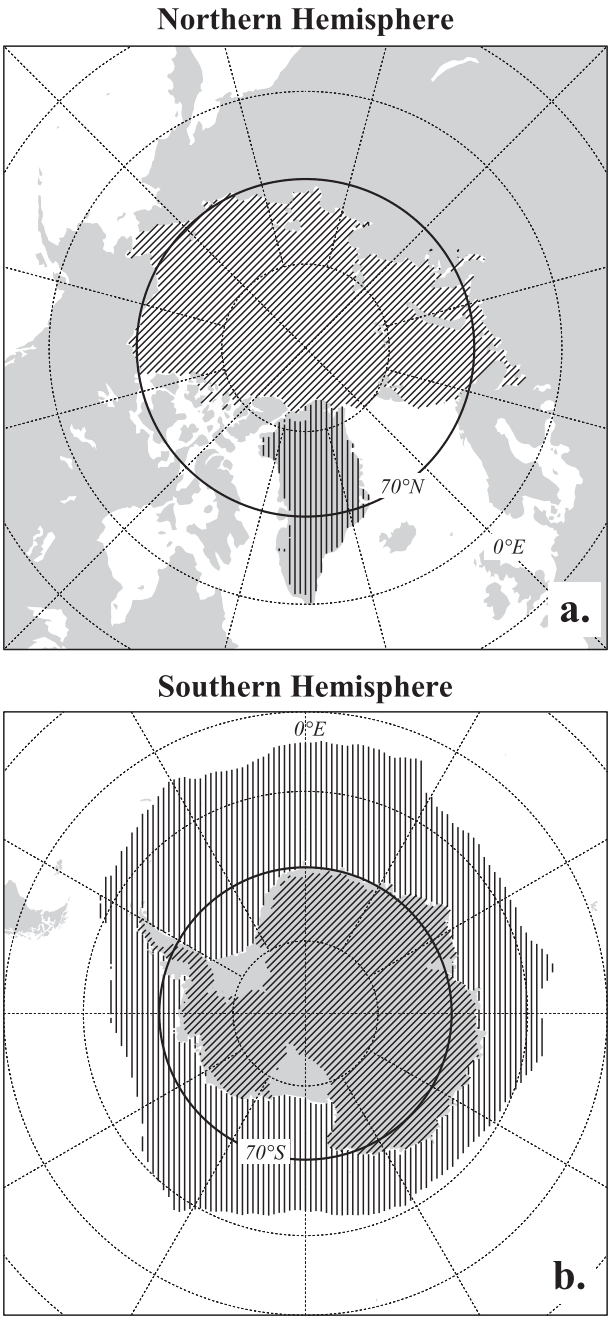

FIG. 1. Regions of study for (a) the Northern Hemisphere and (b) the Southern Hemisphere. Dotted lines are indicated at every 30° of longitude and 10° of latitude. Bold line indicates the 70° parallel. Continental areas are shaded gray. For the Northern Hemisphere, the Arctic Ocean domain is indicated by diagonal hatching, and the Greenland domain by vertical hatching. For the Southern Hemisphere, the Antarctic ice sheet domain is indicated with diagonal hatching, and the Southern Ocean domain by vertical hatching.

TABLE 1. Components of the MERRA atmospheric energy budget (W m^{-2}) for regions defined in Fig. 1. The surface flux F_{sfc} discounts latent heating from solid precipitation. The standard deviation over the 1979–2005 time period is indicated in parentheses.

	$\partial A_E/\partial t$	$-\mathbf{V}\cdot\mathbf{F}_A$	R_{top}	F_{sfc}	$\mathrm{ANA}_{(E)} - Q_{\mathrm{NUM}}$
		70°–90°N			
Jan	−1(11)	110(16)	−173(4)	63(5)	−5(9)
Jul	2(6)	81(8)	2(3)	−68(4)	−13(5)
Mean	0(2)	99(4)	−110(1)	19(1)	−11(5)
		Arctic Ocean			
Jan	−3(13)	106(19)	−176(4)	70(5)	−5(14)
Jul	3(9)	96(10)	−7(4)	−75(6)	−9(6)
Mean	0(2)	99(6)	−114(1)	23(2)	−9(7)
		Greenland			
January	−2(19)	143(26)	−153(6)	−1(4)	4(16)
July	1(8)	118(19)	−48(1)	−40(1)	−32(16)
Mean	0(2)	138(9)	−112(1)	−16(1)	−14(9)
		70°–90°S			
Jan	−1(10)	78(10)	−25(2)	−32(2)	−23(8)
Jul	−10(13)	131(16)	−142(3)	19(2)	−21(10)
Mean	0(1)	118(6)	−101(1)	3(1)	−22(6)
		Southern Ocean			
Jan	2(6)	97(17)	58(10)	−114(9)	−40(17)
Jul	−7(8)	91(15)	−174(1)	82(3)	−11(13)
Mean	0(1)	89(5)	−83(2)	12(2)	−23(5)
		Antarctica			
Jan	−2(10)	80(11)	−41(1)	−21(1)	−21(8)
Jul	−9(12)	135(18)	−134(3)	7(2)	−20(10)
Mean	0(1)	124(5)	−101(1)	−3(1)	−23(5)

fields of the ERA-I were obtained for the years 1989–2005 at a resolution of 0.7° × 0.7°. The CFSR utilizes a coupled atmosphere–ocean–sea ice model for the initial guess field and was produced at T382 spectral resolution. Model variables are produced from 6-h forecasts. Fields from the CFSR were obtained at full spatial resolution.

3. Atmospheric energy budget

a. Analysis increments

Terms of the atmospheric energy budget averaged over the period 1979–2005 from MERRA are shown in Table 1 for the polar regions defined in Fig. 1. The far right column indicates budget adjustment quantities. As noted earlier, artificial moisture filling and chemistry parameterization terms of the energy budget from Eq. (1) have essentially zero magnitude. Not shown, the spatial pattern of the spurious residual Q_{NUM} is characterized by alternating positive and negative values in regions of steep topography. Averages taken over limited areas may produce aliasing of these oscillating values. For example, Q_{NUM} averages 1.5 W m^{-2} over the Greenland ice sheet. But, in general $\mathrm{ANA}_{(E)}$ is the largest adjustment quantity of interest in the atmospheric energy budget, and its spatial

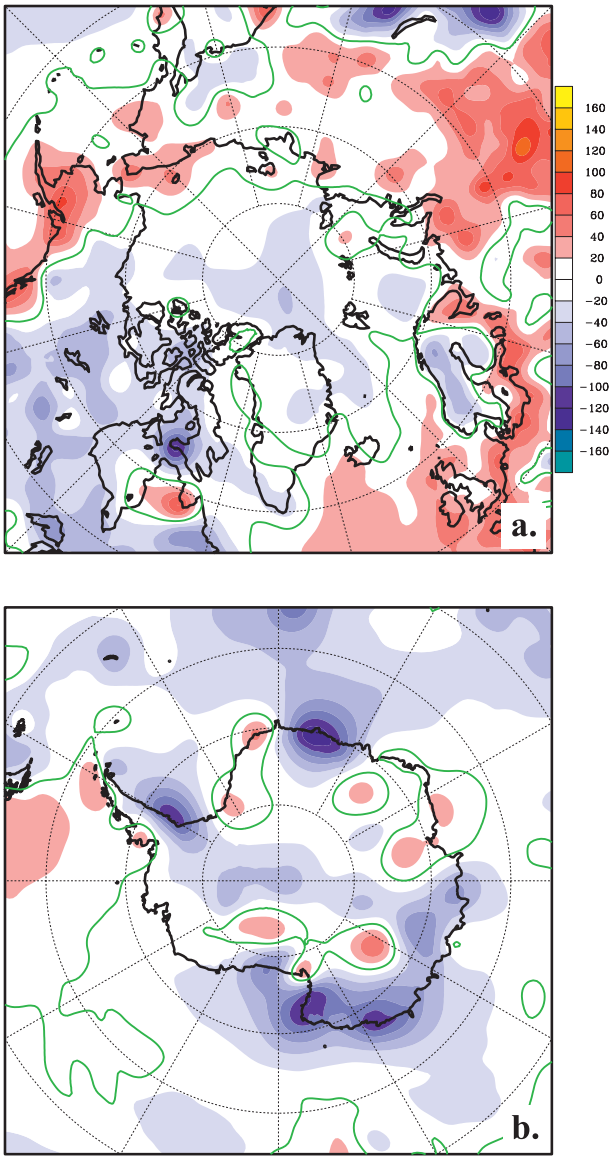

FIG. 2. Annual-average MERRA analysis increments field for the atmospheric energy budget (variable $\mathrm{ANA}_{(E)}$) for (a) the Northern Hemisphere and (b) the Southern Hemisphere. The contour interval is 20 W m^{-2} and the zero contour is indicated with a green line. Dotted lines are shown every 30° of longitude and 10° of latitude.

patterns are shown in Fig. 2. Here positive values indicate an energy deficit in the balance equation while negatives indicate a surplus. The magnitude is a measure of closure obtainable by physical terms. The spatial patterns shown in Fig. 2 are complex, vary with time, and are typically dissimilar to the patterns of the analysis increments for the atmospheric moisture budget shown by Cullather and Bosilovich (2011).

As noted previously, the analysis increment, $\mathrm{ANA}_{(E)}$, is a summation of contributions from latent heat, virtual enthalpy, kinetic, and potential energy terms. Of these four, the contribution from virtual enthalpy is large for monthly and annual averages in both polar cap regions, while the analysis increment from latent heating is also significant for the North Polar cap. For the Northern Hemisphere polar region, negative values for $\mathrm{ANA}_{(E)}$ are found over the Arctic Ocean, while positive values are present over surrounding lower latitudes. Mean annual amounts less than −40 W m^{-2} are present in the vicinity of the North Pole with smaller magnitudes over Greenland and marginal seas. Seasonally, these magnitudes are larger in summer than in winter; however, the values do not approach local imbalances greater than 100 W m^{-2} that are shown for the ERA-40 in Serreze et al. (2007, their Fig. 2). In Fig. 3, the average annual cycle for the net of the adjustment $\mathrm{ANA}_{(E)} - Q_{\mathrm{NUM}}$ is shown using a simple average of months. Again, the spurious numerical adjustment term Q_{NUM} is typically small, and the curve primarily reflects the analysis increment term. For the average over the North Polar cap, $\mathrm{ANA}_{(E)}$ ranges from −4 W m^{-2} in February to −16 W m^{-2} in May and −17 W m^{-2} in June, as shown in Fig. 3a.

In Cullather and Bosilovich (2011), MERRA analysis increments for the atmospheric moisture budget were shown to be characterized by closed contours denoting upper-air stations in coastal Greenland and Antarctica. Although signatures of upper-air station locations are not as evident in the energy budget analysis increment field as in the moisture budget analysis increments, a dipole is apparent in Fig. 2a in the vicinity of Hudson Strait with centers near stations at Kuujjuaq (58°N, 68°W), and Cape Dorset (64°N, 77°W). Patterns shown in Fig. 2a reflect an amalgamation of heterogeneities in the observing system and shortcomings in model skill. Large magnitudes over the Gulf of Alaska are likely indicative of deficiencies in the model representation of the North Pacific storm track, but other features such as differences in sign over land surfaces are not as easily attributable.

The temporal variability of $\mathrm{ANA}_{(E)}$ in the Arctic also differs markedly from the analysis increments field of the atmospheric moisture budget presented in Cullather and Bosilovich (2011). As seen in Fig. 4a, the contribution to $\mathrm{ANA}_{(E)}$ from latent heating is generally constant until the introduction of data from the Advanced Microwave Sounding Unit (AMSU) in November 1998. However the virtual enthalpy analysis increment is also significant for the North Polar cap and is particularly large over the period 1992–97. The relation between variations in the virtual enthalpy analysis increment shown in Fig. 4a and changes to the satellite observing system are not immediately apparent. The magnitude of the total analysis increment $\mathrm{ANA}_{(E)}$ for the North Polar cap energy budget averages less than 10 W m^{-2} for the period 1979–91,

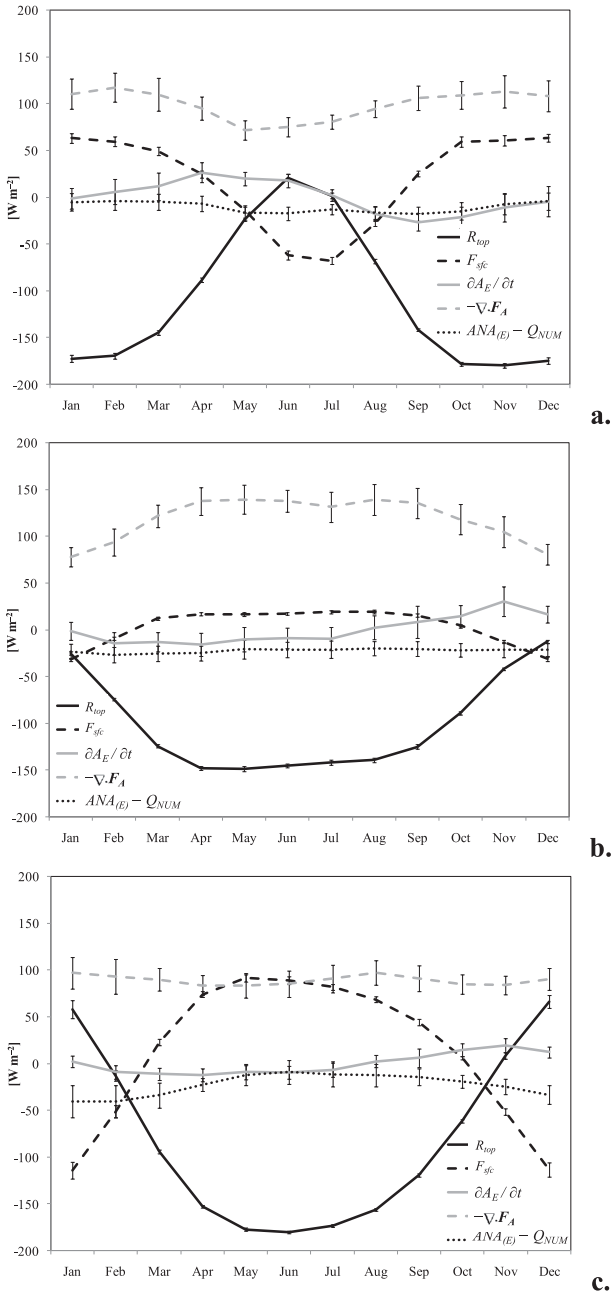

FIG. 3. Annual cycle of atmospheric energy budget components (W m^{-2}) in MERRA for the (a) North Polar cap, (b) South Polar cap, and (c) Southern Ocean domain. Bars indicate ± std dev for the period 1979–2005.

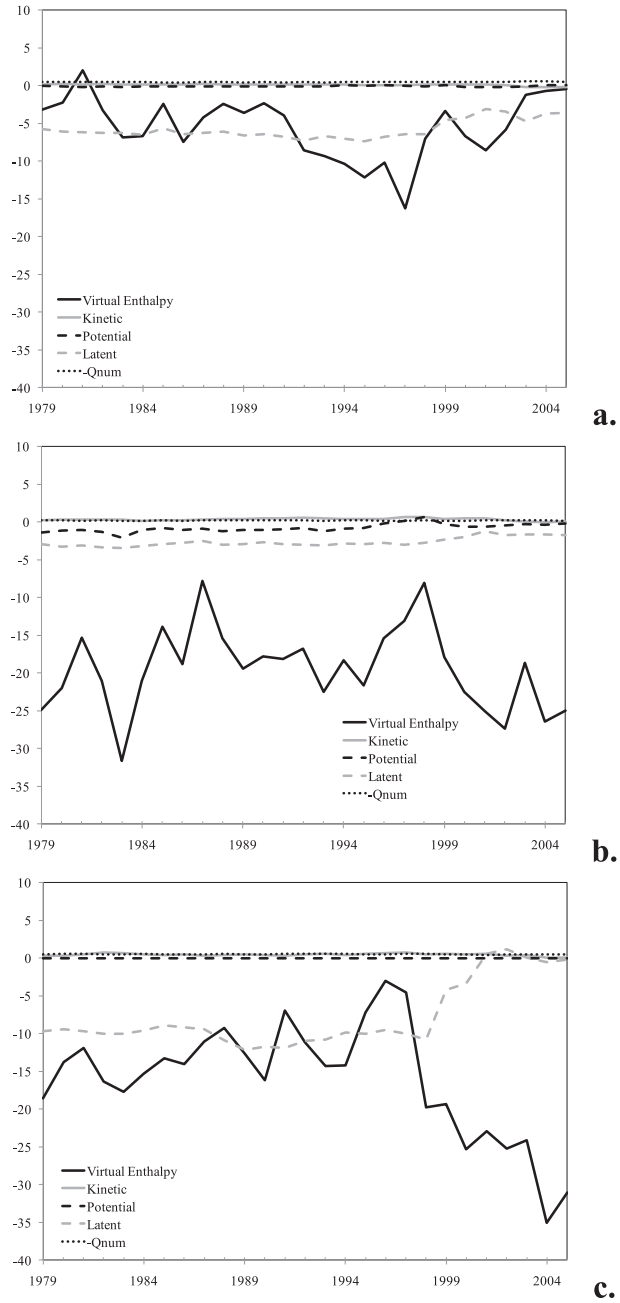

FIG. 4. Time series of annual-averaged virtual enthalpy, kinetic, potential, and latent heat analysis increments and spurious residual term Q_{NUM} (W m^{-2}) for MERRA for (a) North Polar cap, (b) South Polar cap, and (c) the Southern Ocean domain.

18 W m^{-2} over the period 1992–97, and 9 W m^{-2} thereafter.

Shown in Fig. 2b, the spatial pattern of the MERRA analysis increment for the Southern Hemisphere polar region contains larger values than for the Northern Hemisphere. Magnitudes greater than (−)80 W m^{-2} are found over Victoria Land and coastal regions of Queen Maud Land in East Antarctica, while smaller magnitudes are found over the data-sparse lower latitudes of the Southern Ocean. The annual cycle of the analysis increment for the South Polar cap ranges from −27 W m^{-2} in February to −20 W m^{-2} in August and September, as shown in Fig. 3b. For the Southern Ocean domain there is a large annual cycle for the analysis increment, which

ranges from -40 W m^{-2} in January and February to -9 W m^{-2} in June, as shown in Fig. 3c. The year-to-year time series of the analysis increment for the South Polar cap is highly variable and ranges from -37 W m^{-2} in 1983 to -9 W m^{-2} in 1998. As may be seen in Fig. 4b, the dominant contribution to $\mathrm{ANA}_{(E)}$ is from virtual enthalpy. The analysis increment components for the South Polar cap are uncorrelated with those of the North Polar cap, and their relation to changes in the observing system are also not readily apparent. But over the data-sparse Southern Ocean domain, shown in Fig. 4c, a considerable discontinuity in the time series in contributions from latent heat and virtual enthalpy terms occurs in 1998 and is likely associated with the introduction of AMSU data.

b. *Total atmospheric energy tendency*

For both North and South Polar caps, the MERRA total energy tendency is near zero for annual averages and is small for solstice months , as shown in Table 1. But there is an oscillatory annual cycle for the tendency terms as seen in Fig. 3. For the North Polar cap, the tendency term reaches a maximum of 26 W m^{-2} in April and a minimum of -26 W m^{-2} in September. This annual cycle agrees very closely with values from other reanalyses as reported by Porter et al. (2010, average annual range of 57 W m^{-2}), Serreze et al. (2007, annual range of 52 W m^{-2}), and from the observational study of Nakamura and Oort (1988, annual range of 54 W m^{-2}). The rms differences of monthly means with MERRA are 4 W m^{-2} for both NCEP–NCAR and JRA-25 as reported by Porter et al. (2010), less than 1 W m^{-2} for ERA-40 as reported by Serreze et al. (2007), but 10 W m^{-2} for Nakamura and Oort (1988). In general the reanalyses are more similar to each other than to the earlier Nakamura and Oort time series.

For the South Polar cap, the total energy tendency in MERRA ranges from a minimum of -16 W m^{-2} in April to 30 W m^{-2} in November. As seen in Fig. 3b, the annual cycle is less sinusoidal than in the Northern Hemisphere, with the November peak offsetting an average negative tendency that extends from January through July. The rms difference with monthly values reported by Nakamura and Oort (1988) as compared to MERRA is 13 W m^{-2}, although each month is within the standard deviation of MERRA for the 1979–2005 period.

c. *Energy convergence and transport*

For the North Polar cap, the annual cycle of atmospheric energy convergence from MERRA consists of values greater than 100 W m^{-2} during winter months September through March and a minimum of 72 W m^{-2} in May, as seen in Fig. 3a. For comparison, Porter et al. (2010) present annual cycles of energy convergence computed as a residual using several combinations of reanalyses and radiative flux datasets for the period 2000–05, while Serreze et al. (2007) present ERA-40 and NCEP–NCAR reanalysis average monthly values for the period 1979–2001. While there is agreement in having larger energy convergence in winter, there is considerable variability among the datasets on the months of the minimum and maximum value, with May providing a spread of 40 W m^{-2} among the various methods. MERRA values concurrent with these previous studies are found within this large range.

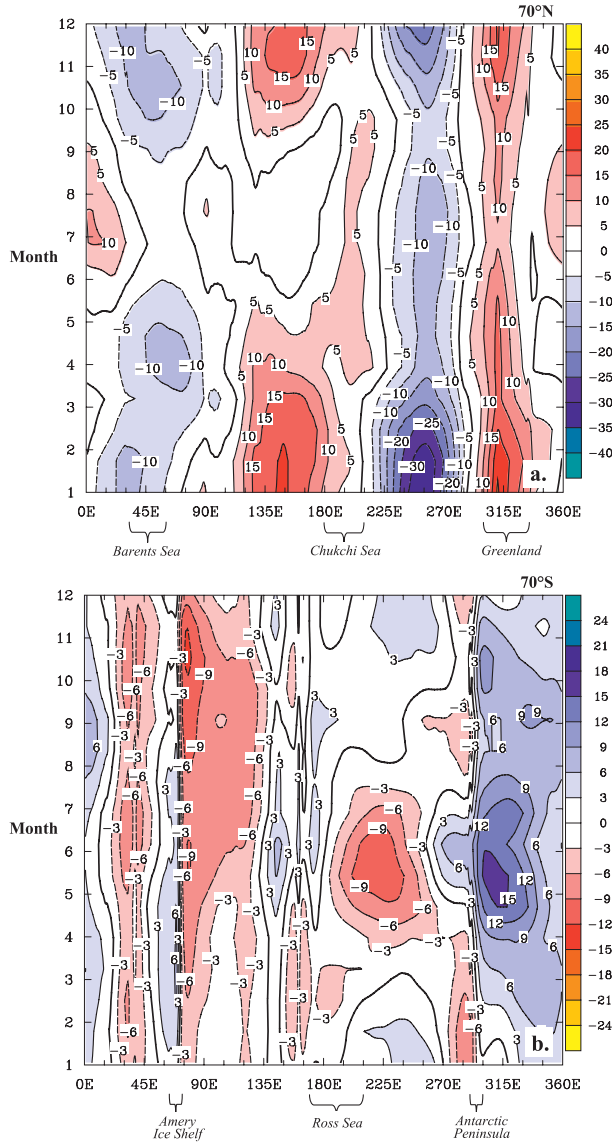

FIG. 5. Average monthly meridional energy transport from MERRA (a) across 70°N, contoured every 5×10^9 W m^{-1}, and (b) 70°S, contoured every 3×10^9 W m^{-1}. Positive values indicate northward transport. Negative values are indicated by dashed contour lines.

Figure 5a shows that the average poleward energy transport across 70°N in MERRA is zonally asymmetric

and is focused at preferred longitudes that are associated with the mean long-wave circulation patterns in the middle troposphere (Serreze et al. 2007). As indicated in the results of Serreze et al., the poleward energy transport is dominated by the sensible and geopotential energy contributions. The latent heat transport (e.g., Sorteberg and Walsh 2008) exhibits a similar spatial distribution as that of the total transport, but reaches maximum magnitude in summer and is smaller by two orders of magnitude. In comparison to energy transports across 70°N from ERA-40 as reported by Serreze et al. (2007), MERRA transports shown in Fig. 5a are comparable but with some differences. First, the poleward (positive) flux centered near 315°E (45°W) has a smaller zonal extent than is shown in Serreze et al.. This may be due to the higher spatial resolution of MERRA and the role of Greenland topography in defining the midtropospheric trough pattern over eastern North America. Second, the wintertime poleward transport near 150°E is shown in MERRA to be greater than 20×10^9 W m^{-1}. This is larger by one contour level (5×10^9 W m^{-1}) than that shown by Serreze et al. (2007) for ERA-40. But in general the average meridional transport patterns of MERRA and ERA-40 are remarkably similar.

Fewer studies of atmospheric energy convergence are available for the Southern Hemisphere. However comparisons to MERRA may be made using the analysis of GCM output in Nakamura and Oort (1988) and the Genthon and Krinner (1998) study of ERA-15 for the period 1979–93. Average energy convergence values for the South Polar cap of 95 W m^{-2} from Nakamura and Oort and 81 W m^{-2} from Genthon and Krinner are both considerably smaller than for MERRA. As seen in Fig. 3b, the annual cycle in MERRA contains a broad maximum over winter months and a short summer period of values less than 100 W m^{-2} in December, January, and February. In contrast the annual cycle of Nakamura and Oort (1988) is generally more sinusoidal. Nakamura and Oort and MERRA monthly energy convergence values are comparable over the months May to October, but MERRA is larger by more than 30 W m^{-2} for all other months, and is larger by 45 W m^{-2} in January. For the study of ERA-15 by Genthon and Krinner (1998), the largest differences with MERRA are in autumn. Energy convergence for the South Polar cap for March–May averages 134 W m^{-2} in MERRA, while Genthon and Krinner reported 79 W m^{-2}. ERA-15 was known to employ a defective ice sheet orography (Uppala et al. 2005), which may contribute to differences between the reanalyses. A visual inspection of Genthon and Krinner (1998) results indicates that the ERA-15 mean annual poleward transport is less than MERRA near 30°E, a point of intersection between the 70°S parallel and the East Antarctic coastal escarpment. For this location, Genthon and Krinner (1998) plot amounts between 2 and 3 ($\times 10^9$ W m^{-1}) while MERRA values are greater than 5×10^9 W m^{-1}. Additionally Genthon and Krinner indicate an annual mean equatorward energy transport in the Ross Sea, while MERRA indicates an average poleward flux. MERRA and ERA-15 share some general characteristics of the meridional energy transport including a directional change with season in the South Pacific region between 180° and 270°E from poleward during winter months to equatorward in summer, as shown in Fig. 5b. The figure also shows an opposing seasonal reversal between 270° and 300°E in MERRA, and this is also shown in Genthon and Krinner (1998).

d. TOA radiative fluxes

For the North Polar cap, MERRA TOA radiative fluxes are compared to published values of ERBE (Serreze et al. 2007) and CERES (Porter et al. 2010). Differences between the two satellite datasets are of interest given recent issues associated with CERES (Loeb et al. 2009; Trenberth et al. 2009). For example, Trenberth et al. (2009) indicate that the global TOA net flux imbalance from CERES differs with best estimates by 5.6 W m^{-2}. Loeb et al. (2009) note further that ERBE radiances have substantial limitations over snow and sea ice, which may contribute to differences between the two satellite products in polar regions. The comparison of MERRA TOA radiative fluxes are thus presented in this context.

As shown in Fig. 3a, the Arctic TOA radiative flux in MERRA is mainly directed upward ($R_{\mathrm{top}} < 0$) with the exception of midsummer months. For the ERBE study period, MERRA and the satellite record both average -110 W m^{-2}. For CERES, the corresponding MERRA average is -112 W m^{-2} and the satellite annual value is -109 W m^{-2}. On monthly time scales, the largest differences are for May, when the MERRA 1979–2005 value of -23 W m^{-2} compares with -53 W m^{-2} in ERBE (Serreze et al. 2007) and -37 W m^{-2} in CERES (Porter et al. 2010). Using MERRA averages concurrent with these satellite records, MERRA is less than satellite estimates for May by 29 W m^{-2} as compared to ERBE and by 12 W m^{-2} as compared to CERES. This seasonal difference between MERRA and satellite observations is consistent with the springtime surface albedo bias, discussed below. In July CERES indicates a net downward TOA flux of 21 W m^{-2} compared to a 1 W m^{-2} upward flux in MERRA and ERBE satellite data. For other months the differences are small.

Table 2 also presents R_{top} values for MERRA in comparison to contemporary reanalyses of the ERA-I and CFSR for the period 1989–2005. As seen in Table 2 for the North Polar cap, the MERRA annual net TOA radiative

TABLE 2. MERRA, CFSR, and ERA-I 1989–2005 average TOA and surface energy flux values (W m^{-2}) for regions defined in Fig. 1. The standard deviation over the time period is indicated in parentheses.

	R_{top}			F_{sfc}		
	MERRA	CFSR	ERA-I	MERRA	CFSR	ERA-I
			70°–90°N			
Jan	−172(4)	−172(5)	−174(4)	64(6)	55(7)	55(7)
Jul	2(3)	−1(3)	2(3)	−69(4)	−87(5)	−78(4)
Mean	−110(2)	−114(1)	−113(1)	19(1)	14(1)	12(2)
			Arctic Ocean			
Jan	−176(4)	−174(5)	−177(4)	70(5)	59(7)	56(5)
Jul	−5(4)	−2(3)	1(3)	−79(6)	−106(8)	−91(6)
Mean	−114(1)	−115(1)	−116(1)	23(1)	12(2)	12(2)
			Greenland			
Jan	−152(5)	−159(5)	−159(5)	0(3)	6(1)	12(3)
Jul	−48(1)	−58(2)	−49(2)	−40(1)	−12(2)	−18(1)
Mean	−112(1)	−120(2)	−116(2)	−16(1)	1(0)	1(0)
			70°–90°S			
Jan	−26(2)	−34(3)	−18(2)	−31(2)	−19(2)	−24(2)
Jul	−142(2)	−147(3)	−147(3)	19(2)	16(4)	13(2)
Mean	−101(1)	−109(1)	−102(1)	3(1)	7(2)	3(1)
			Southern Ocean			
Jan	55(11)	76(5)	74(3)	−111(9)	−145(5)	−137(3)
Jul	−173(1)	−172(1)	−177(1)	81(10)	84(5)	69(4)
Mean	−84(3)	−77(2)	−82(1)	13(2)	3(5)	−2(1)
			Antarctica			
Jan	−41(1)	−54(2)	−37(2)	−21(1)	−2(0)	−6(1)
Jul	−134(3)	−140(3)	−139(3)	7(2)	2(0)	4(1)
Mean	−101(1)	−109(1)	−101(1)	−3(1)	1(0)	0(0)

flux is greater than for the other two reanalyses by 3 and 4 W m^{-2}. Again, the largest differences are for the spring time period. For May R_{top} in ERA-I averages −33 W m^{-2} while the CFSR value is −36 W m^{-2}, and MERRA averages −23 W m^{-2}. Most of this difference is associated with the upwelling shortwave flux. In May MERRA TOA upwelling shortwave flux is less than CFSR and ERA-I by 15 W m^{-2} and 16 W m^{-2}, respectively. It is noted that CFSR incorporates an 11-yr solar cycle while MERRA and ERA-I use climatological solar forcing, and that ERA-I uses a larger solar constant value than MERRA. For the North Polar cap, differences in incoming solar radiation between MERRA and CFSR are as large as ±3 W m^{-2} for a given month, but average less than 1 W m^{-2}. Differences between ERA-I and MERRA are as large as 9 W m^{-2} for a given month and average 3 W m^{-2}.

For the South Polar cap, the TOA net radiative flux remains negative for all months. Comparisons to both ERBE data and values from Nakamura and Oort (1988) indicate that the annual net TOA radiative flux magnitude in MERRA is too large and that the discrepancy is largest during winter months. The 1979–2005 average net flux as shown in Table 1 for MERRA is −101 W m^{-2}. This compares with −90 W m^{-2} from the historical satellite data used in Nakamura and Oort (1988), and −95 W m^{-2} from ERBE for the period February 1985 to April 1989 (Briegleb and Bromwich 1998). The 1979–2005 annual average for R_{top} is by chance equal to the 1985–89 average for MERRA. In the annual cycle, the largest differences with satellite observations are in winter. For the months June–August, the average flux from Nakamura and Oort (1988) is −131 W m^{-2} and from ERBE, −134 W m^{-2}. For MERRA, the corresponding value is −142 W m^{-2} for both 1979–2005 and 1985–89 time periods. In these winter months, the difference between MERRA and satellite values is almost entirely composed of the outgoing longwave component.

Values for the South Polar cap from ERA-I and CFSR reanalyses tend to agree more closely with MERRA than with satellite datasets. For the 1989–2005 period the net TOA radiative flux, shown in Table 2, averages −101 W m^{-2} for MERRA, −109 W m^{-2} for CFSR, and −102 W m^{-2} for ERA-I. The difference between CFSR and the other two reanalyses is attributable to the upwelling shortwave flux component. The CFSR upwelling shortwave flux is greater than the other two reanalyses by more than 15 W m^{-2} in December and January.

Table 2 indicates the standard deviation of the TOA net radiative flux for each reanalysis. Over the Southern Ocean domain abrupt changes in the mean values of two of the reanalyses suggest problems associated with the introduction of AMSU in November 1998. The value for R_{top} in MERRA averages −82 W m^{-2} for the period 1989–99, but this abruptly changes to an average of −86 W m^{-2} for the period 1999–2005. Similarly, the CFSR in the Southern Ocean domain averages −76 W m^{-2} for the period 1989–99, but −79 W m^{-2} for the period 1999–2005.

e. Surface fluxes

1) NORTH POLAR CAP

Figure 6a shows the annual-average surface net heat flux from MERRA for the Northern Hemisphere polar region. Small negative values of between 0 and −5 W m^{-2} are found in a uniform field over nonglaciated land surfaces, consistent with subsurface warming in recent years (Serreze et al. 2007). Over the central Arctic Ocean the MERRA net surface flux is positive as expected, but is exceptionally large. Values greater than 15 W m^{-2} are found in the central Arctic and greater than 20 W m^{-2} in the approaches to the North Atlantic. These annual values are extraordinary and likely not realistic. For example, Serreze et al. (2007) deduced an Arctic annual net surface flux of 6 W m^{-2} using available estimates of ocean heat transport values, while Nakamura and Oort (1988) derived a value of 2.4 W m^{-2} for the North Polar cap

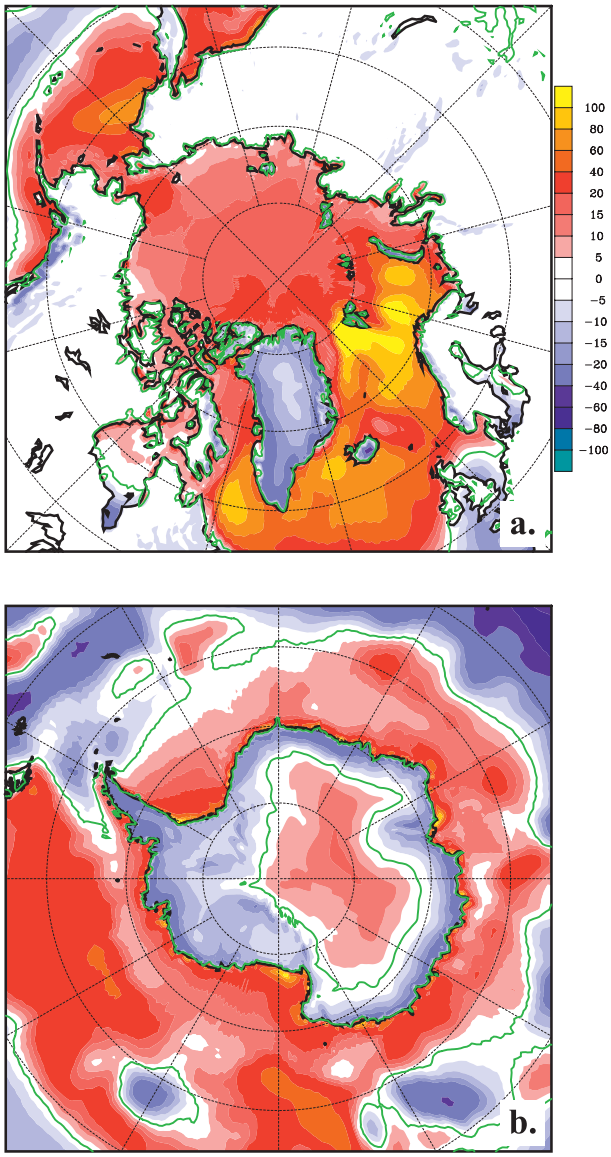

FIG. 6. Annual-average net surface heat flux from MERRA (positive upward) for (a) the Northern Hemisphere and (b) the Southern Hemisphere. Shading is plotted at intervals of 20 W m^{-2} and for the levels −10, −5, 0, 5, and 10 W m^{-2}. The zero contour is indicated with a green line. Dotted lines indicate every 30° of longitude and 10° of latitude.

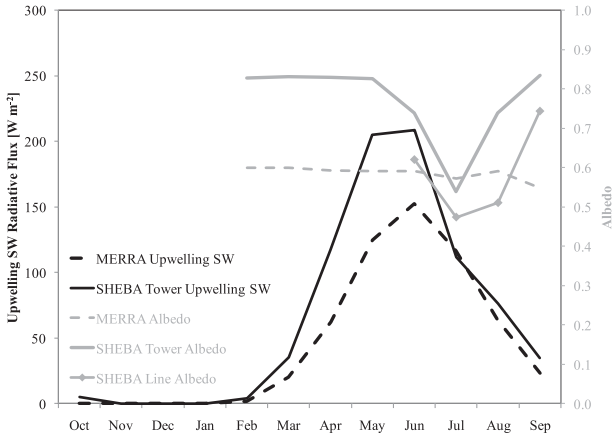

FIG. 7. Monthly averaged surface albedo (gray) and upwelling shortwave radiative flux (dark, W m^{-2}) for SHEBA observed (solid) and corresponding MERRA values (dashed) for October 1997 to September 1998. "Tower" values are from downward-pointing pyranometer measurements, while "line albedo" values are from surface measurements along a 300-m line.

using atmospheric transports and TOA radiative fluxes from satellite data.

The MERRA net surface flux averaged annual cycle is shown in Fig. 3a for the North Polar cap. Comparison with previous studies indicates largest discrepancies occurring in summer months. The July average MERRA net surface flux of −68 W m^{-2} compares with −85 W m^{-2} for ERA-40 (Serreze et al. 2007) and −86 W m^{-2} for JRA-25 (Porter et al. 2010). Similar differences are found between MERRA and contemporary reanalyses, as shown in Table 2. For the concurrent 1989–2005 averaging period, the July net surface flux for the North Polar cap is −87 W m^{-2} for the CFSR and −78 W m^{-2} for ERA-I.

Discrepancies in the surface flux fields are evaluated using observations from the Surface Heat Budget of the Arctic (SHEBA) ice camp study in the Beaufort Sea from October 1997 to October 1998 (Uttal et al. 2002). MERRA is evaluated with a compilation of observed SHEBA radiative and turbulent flux measurements by Duynkerke and de Roode (2001). Rawinsonde data and pressure reports from the ship (Canadian Coast Guard icebreaker CCGS *Des Groseilliers*) and surrounding stations and buoys were assimilated in MERRA. Surface temperature is not assimilated. Comparisons are made using the nearest MERRA grid point to the reported hourly drift camp position (e.g., Francis et al. 2005; Gorodetskaya and Tremblay 2008; Inoue et al. 2006; Dorn et al. 2007; Sedlacek et al. 2007). Over the full record, the average distance from the observing location to the grid point center ranged from 0 to 28.8 km with an average of 15.1 km as the station drifted through 88 unique MERRA points. For this data source, SHEBA latent heat flux observations were limited and are not considered. The remaining observed energy budget components indicate a positive (upward) bias in MERRA of 18 W m^{-2} for the months October–April, −1 W m^{-2} for May, and small positive biases for the following summer months.

There are three basic results of this comparison. As shown in Fig. 7, substantial differences in the upwelling shortwave radiative flux result from an overly simplistic representation of sea ice properties. Sea ice albedo is set to a fixed value of 0.60 for MERRA. SHEBA tower

measurements indicate a much higher albedo in spring with monthly averages of 0.83 in March–May and 0.74 in June. Apart from the tower flux measurements, a line of surface albedo observations made during SHEBA provide a range of values that are dependent on the surface ice conditions. The average of these surface observations is shown in Fig. 7 for June–September 1998. Albedos from tower measurements in May 1998 are consistent with area-averaged surface and aircraft observations. For example, Curry et al. (2001) note that albedo for April and May at the SHEBA site averaged 0.84, that the melt season lasted from late May to mid-August, and that winter–spring albedo values were again reached in late September. The differences shown in Fig. 7 are associated with the sea ice albedo, and not discrepancies in the Reynolds sea ice fraction used in MERRA. The MERRA gridded ice fraction for the SHEBA location remained near 1.00 until mid-May 1998 and decreased to a low of 0.86 in late summer. This is reflected in the small variations in the albedo curve for MERRA shown in Fig. 7. The difference with observed albedo contributes to an underestimate in the upwelling shortwave flux in MERRA of 55 W m^{-2} in April, 80 W m^{-2} in May, and 56 W m^{-2} in June. In late summer the observed surface albedo is degraded by melting and becomes comparable to the MERRA fixed value. In late autumn freezing and the introduction of solid precipitation again produces surface albedo differences between MERRA and observation; however, the incoming solar flux is reduced and the impact on the upwelling shortwave is less consequential. The difference with observation in the upwelling shortwave radiative flux for May is the largest of any monthly budget component.

The second result is a response in other MERRA surface energy budget terms in May to the albedo bias. Surface temperatures over ice in MERRA are determined via energy balance, and the underestimate of surface albedo results in a perceived increased absorption of solar energy and a surface warming. This likely results in a MERRA sensible heat flux bias of 16 W m^{-2} for May. Other than the April–June period, the MERRA sensible heat flux difference with SHEBA observations is only 2 W m^{-2}. Additionally, a springtime negative bias with SHEBA observations is found for the downwelling shortwave radiative flux. MERRA downwelling shortwave is underestimated by 36 W m^{-2} in April, 37 W m^{-2} in May, and 25 W m^{-2} in June. In other months this difference is about 1 W m^{-2}. A large fraction of this amount is likely attributable to surface albedo through the re-reflectance of the biased upwelling shortwave flux in the presence of low clouds. A portion of the amount may also be due to a redistribution of cloudiness in the atmospheric column resulting from anomalous surface warming, and from general deficiencies in the representation of cloud properties. Finally, the MERRA upwelling longwave flux is overestimated by 20 W m^{-2} in April and 19 W m^{-2} in May in comparison to SHEBA observations. The large May bias in upwelling shortwave and longwave radiation is then compensated for by biases in other fluxes to produce the surface net energy flux bias of -1 W m^{-2}.

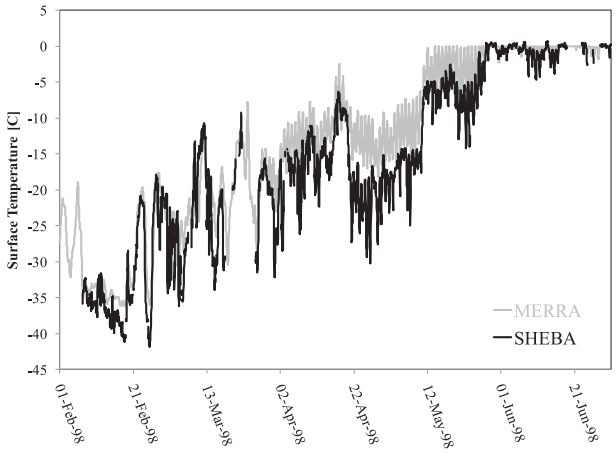

FIG. 8. Hourly surface temperature (°C) from SHEBA and corresponding values from MERRA for the period 1 Feb 1998–30 Jun 1998.

Shown in Fig. 8 is a time series of hourly surface temperature in comparison to SHEBA observations. A temperature bias in spring is readily apparent with a difference of greater than 3.5°C in April and May before the freezing value is reached in late May. In particular, the period 19 April–10 May shows an average bias of 6.1°C in MERRA. But, for daily averages there is a good correlation between MERRA and observation for the period shown (r = 0.95). It may also be seen in Fig. 8 that the diurnal cycle in MERRA temperature has an amplitude between 2° and 10°C, which begins abruptly on 28 March and continues unabated until the freezing point is reached in June. The observed SHEBA diurnal cycle has a similar amplitude; however, the cycle is not as regular as in MERRA and there are periods of considerable interruption, perhaps due to synoptic variability. These differences are suggestive of deficiencies in MERRA boundary layer parameterizations.

An event of particular interest during SHEBA was the first rainfall event on 29 May 1998, which initiated the melt season (Curry et al. 2001; Perovich et al. 2003). As seen in Fig. 8, the observed surface temperature reached 0°C within 2 days of this event, while MERRA temperatures first reach 0°C on 11 May, some 18 days earlier. Although observed latent heat fluxes are not available for this SHEBA dataset, it is noted that the corresponding MERRA latent flux increased from a daily average of

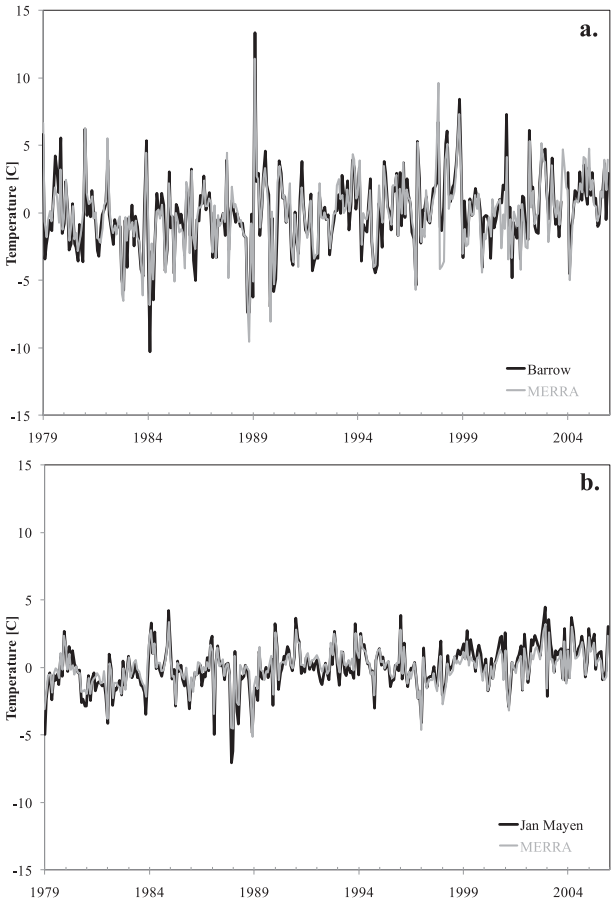

FIG. 9. Time series of monthly averaged near-surface station air temperature anomaly (°C) and corresponding MERRA values for (a) Barrow (71°N, 157°W) and (b) Jan Mayen (71°N, 9°W).

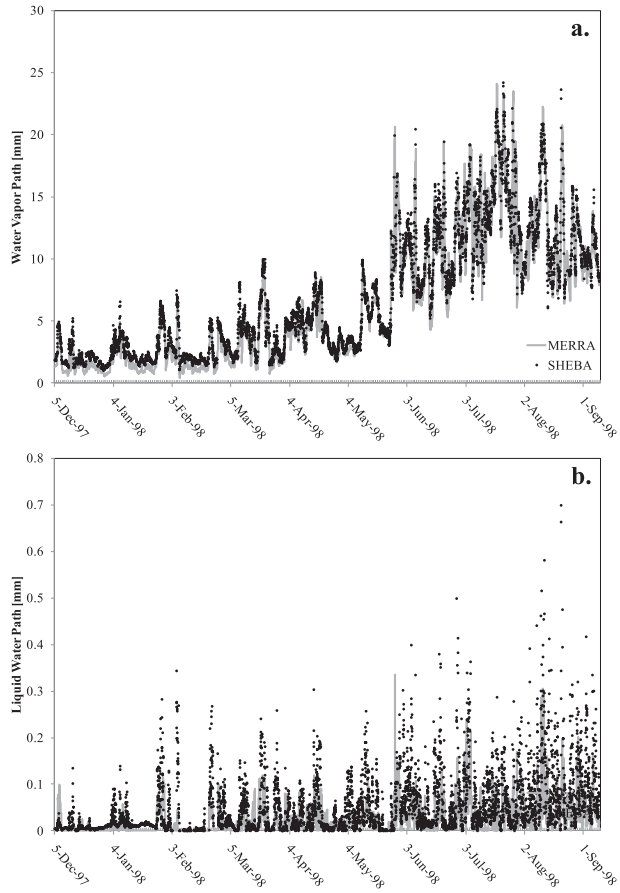

FIG. 10. Hourly (a) precipitable water and (b) liquid water path (mm) from SHEBA microwave radiometer and corresponding MERRA values.

15 W m^{-2} on 10 May to an average of 22 W m^{-2} for the period 12–27 May before decreasing to 1 W m^{-2} with the precipitation event on 29 May. As this case study illustrates, the presence of a warm surface bias creates an inability to represent episodic spring melting events.

Springtime air temperature biases are found at Arctic station locations as well. For example, a comparison with Sachs Harbor (72°N, 125°W), over the period 1979–2005 indicates an average of 4.9°C difference for April but only 1.9°C for the months August through March. A comparison with Barrow (71°N, 157°W), similarly indicates an average bias in MERRA of 3.6°C for the spring months of March–May and 0.9°C for other months. But as shown in Fig. 9, MERRA performs well in a comparison of monthly anomalies. The correlation between temperature anomalies at Barrow and Jan Mayan (71°N, 9°W), is 0.99 for both stations.

The third result from the comparison with SHEBA is an annual-average negative bias in the downwelling longwave radiative flux of 12 W m^{-2}. Consistent with the spring near-surface warm temperature bias, this underestimate of the downwelling longwave flux in MERRA is near zero in April and less than 7 W m^{-2} in May, but is large in other seasons. This quantity leads to the overall positive bias in the net surface flux for summer, autumn, and winter months. As with the springtime downwelling shortwave radiative flux bias, an inadequate representation of cloud properties is implied. To evaluate this further, comparisons were made between MERRA and SHEBA hourly microwave radiometer retrievals over the period from 5 December 1997 to 9 September 1998. More than 5000 observations were made over the period. Retrievals of precipitable water compare remarkably well to MERRA values, as seen in Fig. 10a, although differences are apparent for small quantities in winter. For monthly intervals, the correlation between MERRA and the hourly microwave radiometer precipitable water retrievals ranges from $r = 0.87$ in December 1997 to $r = 0.96$ in May 1998. A consistent bias of 0.6 mm in monthly averages is found, which amounts to 31% of the observed average for January but only 3% for July. In contrast, the comparison to

retrieved liquid water content shown in Fig. 10b is less favorable. Cloud liquid water from the SHEBA microwave radiometer ranges from an average of 0.017 mm in January 1997 to 0.106 mm in August 1998. Typical MERRA values are about 45% of microwave radiometer amounts. Although large discrepancies have been noted between SHEBA microwave radiometer values for liquid water path and simultaneous aircraft measurements (Lin et al. 2001), the differences between MERRA and SHEBA values exceed 50%. Additionally, the correlations of hourly liquid water path values with MERRA over monthly time intervals are low and range from $r = 0.14$ in April 1998 to $r = 0.55$ in January 1998. The presence or absence of cloud liquid water significantly alters the downwelling longwave radiative flux. An underestimate of cloud liquid water in MERRA is qualitatively consistent with differences in the surface net flux with observation.

Comparisons with MERRA for the Arctic are also conducted using the CFSR and ERA-I reanalyses. Using monthly values collocated with the SHEBA ice drift camp, it is noted that surface albedo varies seasonally and interannually in both CFSR and ERA-I. In agreement with SHEBA, both CFSR and ERA-I have sea ice albedos greater than 0.8 for April 1998, and values decrease with the onset of the summer melt season. This decrease occurs more rapidly in both CFSR and ERA-I than for tower observations, but is within the lower range given by SHEBA line albedo measurements. The June 1998 albedo is 0.59 for MERRA, 0.65 for CFSR, 0.69 for ERA-I, 0.74 for the SHEBA tower observation, and 0.62 for the line observation. All three reanalyses underestimate the downwelling longwave radiative flux over winter months in comparison to SHEBA. For the period October 1997 to May 1998 this flux is underestimated by 5 W m^{-2} in ERA-I and 18 W m^{-2} in CFSR. Finally, the November 1997 to March 1998 average sensible heat flux observed at SHEBA is less than 1 W m^{-2}. This compares with 3 W m^{-2} in MERRA, −7 W m^{-2} in ERA-I, and −21 W m^{-2} in CFSR.

2) SOUTH POLAR CAP AND SOUTHERN OCEAN

Turning to the Southern Hemisphere, the annual-average net surface heat flux for the South Polar cap is shown in Fig. 6b. Of immediate concern is the anomalous nonzero field over Antarctica. Over grounded ice, the MERRA subsurface energy flux is determined by the prognostic temperature for a 7-cm (water equivalent) surface ice layer and a deep layer temperature at 2-m depth that is fixed at 230 K. Thus, the location of the zero contour over Antarctica in Fig. 6b exactly matches the annual-average 230 K surface temperature isotherm. Observations from automatic weather stations indicate that annual mean subsurface conductive heat fluxes are not significant (e.g., Reijmer and Oerlemans 2002), and annual surface energy flux patterns in MERRA over Antarctica (as well as Greenland) are erroneous.

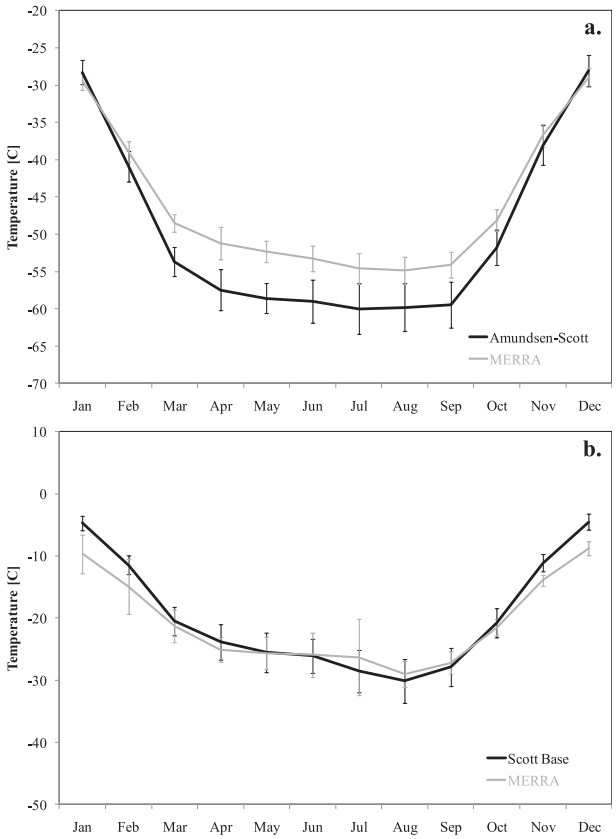

FIG. 11. Average annual time series for near-surface station temperature (°C) and corresponding MERRA values for (a) Amundsen–Scott (90°S) and (b) Scott Base (78°S, 167°E). Bars indicate the standard deviation of monthly values over the period 1979–2005.

The MERRA annual surface net energy flux in Antarctica is produced from a complementary, but unbalanced, distribution of downward (negative) turbulent and upward (positive) radiative fluxes. The turbulent flux is principally composed of sensible heat. The annual-averaged sensible heat flux over the ice sheet is uniformly negative and is approximately contour-parallel with topography, with magnitudes greater than (−)60 W m^{-2} along the East Antarctic coastal escarpment decreasing to less than (−)10 W m^{-2} over the central plateau. The annual mean net radiative flux field in MERRA is spatially more uniform than the turbulent fluxes, with values ranging from 25 to 35 W m^{-2} for East Antarctica and smaller positive values over West Antarctica. This results in the imbalances in the net surface energy flux as shown in Fig. 6b. These errors in the net surface energy flux are related to near-surface temperature biases. As shown in Fig. 11, there is a considerable wintertime warm bias of

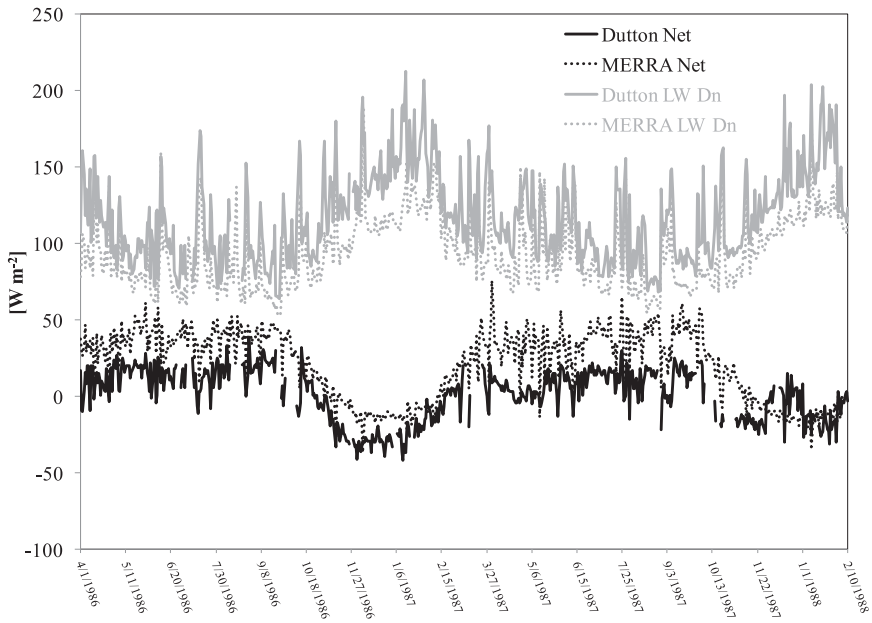

FIG. 12. Time series of daily downwelling longwave flux and the net radiative flux (positive upward) (W m^{-2}) from Dutton et al. (1989) and corresponding values from MERRA for 90°S.

5°C at Amundsen–Scott Station (90°S), while a summer cold bias of 5°C is found at Scott Base (78°S, 167°E). A visual inspection of satellite-derived surface air temperatures in Comiso (2000) indicates that a summer cold bias extends over the embayment regions.

Surface radiative fluxes in MERRA are examined using the South Pole observations of Dutton et al. (1989), who recorded daily mean radiative flux components from April 1986 until February 1988. Over this period, the observed net radiative flux as averaged for an annual time period is 2 W m^{-2}, while the corresponding value for MERRA is 20 W m^{-2}. The concurrent MERRA annual sensible heat flux at South Pole is -10 W m^{-2}. This leaves an imbalance in the net surface energy flux of 10 W m^{-2}, which agrees with the 1979–2005 average shown in Fig. 6b.

As seen in Fig. 12, the net radiative flux differences between MERRA and South Pole observations are largest in winter. From April to October, the net radiative flux is primarily longwave, and is found to be 10 W m^{-2} in observation, but 35 W m^{-2} in MERRA. This bias in MERRA of 25 W m^{-2} in net longwave flux remains consistent throughout the annual cycle. Similar to the results for the comparison with SHEBA observations in the Arctic, a negative bias in the downwelling longwave radiative flux is present throughout the 22-month period of available observations, as shown in Fig. 12. The underestimate in MERRA in comparison to the observed downwelling flux is 24 W m^{-2} for the averaged annual cycle, but is as large as 39 W m^{-2} in January. Differences with observation in the MERRA upwelling longwave flux are largest in winter, and this produces the consistent net longwave flux bias throughout the annual cycle.

A compensating bias in the net shortwave flux reduces the overall net radiative flux bias in summer. For January the observed net shortwave flux is -70 W m^{-2}, while the corresponding MERRA value is -91 W m^{-2}. Unlike results presented for the Arctic, small differences between the MERRA albedo for land ice (fixed at 0.775) and observation do not fully account for differences in the shortwave flux.

Comparisons of MERRA 1979–2005 averaged surface energy budget components have been made with Antarctic station values compiled by King and Turner (1997) to assess the representativeness of the South Pole evaluation. Values compiled by King and Turner (1997) reflect studies of opportunity and do not account for interannual variability. Comparisons of MERRA averages with observations at the South Pole and at Halley Station (76°S, 26°W), indicate underestimates of the net radiative flux by MERRA for winter, similar to the comparison with Dutton et al. (1989). At the South Pole, MERRA net radiative surface cooling for June–August of 36 W m^{-2} exceeds the observed value of 21 W m^{-2} (Carroll 1982). For the sensible heat flux, comparisons with previous values are not consistent. From the observations of Dutton et al. for the South Pole, it is noted that an annual-average sensible heat flux of -2 W m^{-2} is implied to balance the observed net radiative flux and that the corresponding MERRA sensible heat flux is -10 W m^{-2}. In contrast, the sensible flux value from

Carroll (1982) is -19.4 W m^{-2}. At Mizuho Station (71°S, 44°E), MERRA sensible heat flux average values of -47 W m^{-2} for July and -19 W m^{-2} for December compare with observational values of -37 and -25 W m^{-2} for July and December, respectively (Ohata et al. 1985).

Table 2 presents a comparison of net surface flux values for the South Polar cap. Not shown, both the ERA-I and the CFSR correctly depict a near-zero annual net flux field over the Antarctic ice sheet, while erroneous regions of opposite sign in MERRA F_{sfc} fortuitously cancel in the area average. Monthly values of surface radiative flux components from CFSR and ERA-I are also compared to the 1986–88 values from Dutton et al. (1989) for the South Pole. The ERA-I currently begins in 1989, so 1989–2005 averages were used. In general, the monthly net surface radiative fluxes of the three reanalyses are more similar to each other than to observation. The net upward radiative flux is overestimated by 18 W m^{-2} for MERRA, 16 W m^{-2} for ERA-I, and 20 W m^{-2} for CFSR. Similar to MERRA, a large part of the difference between ERA-I and South Pole observations is due to an underestimate of the downwelling longwave component. For the annual average, the ERA-I downwelling longwave flux is underestimated by 15 W m^{-2}. For the CFSR, the upwelling longwave flux is overestimated for winter months March–September by 21 W m^{-2}, and this provides a significant contribution to annual net flux differences.

The spatial patterns of Fig. 6b are of interest over the Southern Ocean. In the annual mean, MERRA indicates a net loss of energy from the ocean to the atmosphere south of 60°S that increases in magnitude near the continent. Farther north there is a marked asymmetry within the 50°–60°S zone, with net energy loss from ocean to atmosphere in the Pacific sector and energy gains elsewhere. Embedded within the Pacific sector are two regions of net energy gain from atmosphere to ocean that correspond to meanderings of the Antarctic Polar Front—as it crosses the Southeast Indian Ridge near 145°E and the Pacific–Antarctic Ridge near 145°W (e.g., Moore et al. 1999). The Pacific sector region of ocean heat loss to the west of South America is associated with deep winter mixed layers formed by the wintertime oceanic convection that produces Subantarctic Mode Water (SAMW) (I. Cerovecki 2010, personal communication). Josey (2009; S. A. Josey 2011, personal communication) noted the zonal asymmetry in the net surface heat flux in NCEP and ECMWF reanalyses but found that coupled models produce a more zonally uniform field. Josey (2009) concluded that the sign of annual mean surface heat exchange over much of the region is not known. Depictions of the net surface flux in ERA-I and CFSR over the Southern Ocean differ with MERRA. The coastal zone of heat loss from the ocean to the atmosphere in both ERA-I and CFSR is more closely confined near the continent than in MERRA. Similar to MERRA, ERA-I indicates an annual mean net positive energy flux from ocean to atmosphere in the Pacific Ocean sector of the 50°–60°S zone, while CFSR indicates negative values between 0 and -15 W m^{-2} that are smaller in magnitude than for the rest of the zone.

The annual cycle of the net surface flux for the Southern Ocean is shown in Fig. 3c. Okada and Yamanouchi (2002) estimated the surface energy budget for the Southern Ocean bounded by 60° and 70°S as a residual using TOA ERBE radiation and divergence terms of the ECWMF operational analyses. A seasonal asymmetry in the net surface flux was highlighted, which was found to abruptly peak in May with a maximum of 116 W m^{-2}. Okada and Yamanouchi attributed this asymmetry to the latent heat release resulting from sea ice formation. As seen in Fig. 3c, the MERRA surface energy flux over the Southern Ocean sea ice domain is also asymmetric and peaks in May at 98 W m^{-2}; however, the maximum is not as striking as was found for the ECMWF analyses. In examining the autumnal surface turbulent fluxes in MERRA, it is found that the total latent heat flux is a maximum for the domain in April with 33 W m^{-2}. The latent heat flux then diminishes over ice covered winter months, with a second maximum of 28 W m^{-2} in November.The MERRA sensible heat flux reaches its annual maximum of 21 W m^{-2} in May and generally reflects the shape of total surface net flux. The asymmetry in the annual cycle for the MERRA net surface flux, as shown in Fig. 3c, is then principally due to seasonal changes in the sensible heat flux. In reanalyses, sea ice cover is prescribed from observational fields. The latent heat flux arising from ice formation is manifest as the net conductive flux at the atmosphere–ice interface. In this context, MERRA and the results of Okada and Yamanouchi (2002) are broadly consistent.

4. Summary and discussion

MERRA reproduces the basic patterns of energy flow in the polar atmosphere as they are known. As shown in Fig. 3, the polar regions are marked by a convergence of energy from lower latitudes for all months and a loss of energy at the top of the atmosphere for the most of the year. In the Arctic, reductions in the TOA shortwave radiative flux in autumn produce a negative tendency in the atmospheric column total energy throughout the period from August to January that is moderated by contributions from the net surface flux and increased energy transport from lower latitudes in winter (Serreze et al. 2007). In the Antarctic, this seasonal progression is less sinusoidal, with the net TOA radiative flux remaining

negative throughout the year, and an extended winter period in the energy budget components extending from April to September.

Despite reproducing these essential features, MERRA energy budgets for the Arctic and Antarctic contain substantial errors owing to overly simplistic physical parameterizations, including sea ice albedo, the surface heat budget over permanent land ice, and cloud radiative properties. A fixed sea ice albedo results in a springtime upwelling shortwave radiative surface flux underestimate of up to 80 W m^{-2} in the Arctic, and annual net surface flux imbalances of up to 30 W m^{-2} are found locally over polar ice sheets. Deficiencies in MERRA sea ice characteristics are not dissimilar from those described in Bretherton et al. (2000) for ECMWF analyses produced during SHEBA, and indeed the discrepancies in surface shortwave radiative fluxes are similar. Spring is a critical period for evaluation of surface flux fields in the Arctic, and differences between MERRA shortwave surface radiative fluxes with observation are most prominent in May. Over the data-sparse Southern Ocean, discontinuities in the time series of TOA radiative fluxes coincide with the introduction of AMSU satellite data in November 1998 and are therefore spurious. Elsewhere, interannual variability of the analysis increments term $ANA_{(E)}$ is large but not as easily linked to changes in the observing system.

MERRA nevertheless compares favorably to previous studies of energy budget components produced from state and dynamical variables. Atmospheric energy convergence and the spatial distribution of transport along the 70° parallel compare closely with previous studies in the Northern Hemisphere, while estimates for the South Polar cap are qualitatively similar but may also be seen as an update to studies based on earlier analyses. The total atmospheric energy tendency in polar regions also compares favorably to previous studies.

Credible estimates of the atmospheric energy budget in polar regions continue to be a significant challenge owing to changes in the observing system and complex energy feedback mechanisms that are associated with the high latitudes. Evaluation using both representative point location observations and previous area-averaged estimates such as those used in this study are valuable for providing a straightforward appraisal of reanalyses. The MERRA system is an important product because of its alternative construction, including a nonspectral background model and its emphasis on NASA satellite products. An important concept used in MERRA is the employment of analysis increments for identifying differences between observations and the background analysis system. Inconsistencies in atmospheric budgets are quantified in the analysis increments, which is one measure of confidence. ERA-I and CFSR reanalyses are found to utilize seasonal variations in sea ice albedo and have realistic annual-mean surface heat fluxes over ice sheets. However these reanalyses are also found to have significant discrepancies with observed surface and TOA energy fluxes. In particular, sensible heat fluxes from CFSR are large in comparison to SHEBA observations, while all three reanalyses overestimate the annual surface net radiative flux at South Pole by 16–20 W m^{-2}. These disagreements underscore the challenge of the high-latitude energy budget problem. In addition, the evaluation of TOA fluxes is problematic owing to discrepancies in available satellite-derived studies, and there remains a need for representative, validating in situ observations of turbulent fluxes in high latitudes.

Several points for further examination are indicated by this study. The further characterization of analysis increments including their vertical distribution is useful for attributing nonclosure of the energy budget to particular deficiencies in available observations. There is a particular need for diagnosing deficiencies in cloud radiative properties for reanalyses in polar regions—this may be accomplished with available satellite and in situ products. Further consideration should also be given to the evaluation of surface energy fluxes over Arctic terrestrial watersheds in light of the results of Reichle et al. (2011). Coupled model simulations for the Intergovernmental Panel on Climate Change (IPCC) are additional tools for understanding the polar energy budget (e.g., Sorteberg et al. 2007). While reanalyses have typically served as a validation for climate models, comparisons of multiple reanalyses with the output of models from the upcoming IPCC Fifth Assessment, including short-term decadal simulations, may provide unique insight and improve our knowledge of various budget components.

Uncertainty in estimates based on reanalyses has been the subject of investigation over an extended period of time. Uncertainty is typically defined as the standard deviation of a sufficiently large number of measurements of the same quantity by the same method (e.g., Glickman 2000). Uncertainty may be illustrated through the sampling of available estimates, and the mean values provided in Table 2 serve this purpose. Comparisons with earlier analysis-based studies are instructive with the knowledge that the interannual variability of budget components may be large. In the case of atmospheric reanalyses, however, errors are typically systematic owing to the use of similar sets of observations, model parameterizations, and assimilation methods (Langland et al. 2008; Dee 2005).

Langland et al. (2008) writes that there is no definitive way to determine which reanalysis is closer to ''truth'' because exact information about observation or analysis error is not available. As noted by Dee (2005), persistent

spatial and temporal patterns in analysis increments are a clear indicator of bias in reanalyses. The distribution of analysis increments in MERRA thus facilitates a more detailed understanding of reanalysis bias than has been previously available.

Acknowledgments. Data from the Surface Heat Budget of the Arctic Ocean experiment (SHEBA) were obtained from the University of Washington Department of Atmospheric Sciences, Seattle, Washington. Reference Antarctic Data for Environmental Research (READER) is a project of the Scientific Committee on Antarctic Research (SCAR) and were obtained from British Antarctic Survey (BAS), Cambridge, United Kingdom. Arctic station values from the Integrated Surface Database (ISD) and the Integrated Rawinsonde Global Rawinsonde Archive (IGRA) were obtained from the National Climate Data Center, Asheville, North Carolina. The ERA-I was obtained from the Data Support Section at the National Center for Atmospheric Research. The CFSR was obtained from the National Climate Data Center. This study was funded by grants from the NASA Modeling Analysis and Prediction Program (MAP) and the NASA Energy and Water Cycle Study (NEWS) to the second author.

APPENDIX

Representation of the Atmospheric Energy Budget Using MERRA Variables

The MERRA variables are given as follows.

DQVDT_DYN	Vertically integrated water vapor tendency for dynamics, kg m^{-2} s^{-1}
DQVDT_PHY	Vertically integrated water vapor tendency for physics, kg m^{-2} s^{-1}
DQVDT_ANA	Vertically integrated water vapor tendency for analysis, kg m^{-2} s^{-1}
DQIDT_DYN	Vertically integrated ice water tendency for dynamics, kg m^{-2} s^{-1}
DQIDT_PHY	Vertically integrated ice water tendency for physics, kg m^{-2} s^{-1}
DQIDT_ANA	Vertically integrated ice water tendency for analysis, kg m^{-2} s^{-1}
DQVDT_CHM	Vertically integrated water tendency for chemistry, kg m^{-2} s^{-1}
DQVDT_FIL	Artificial "filling" of water vapor, kg m^{-2} s^{-1}
DQIDT_FIL	Artificial "filling" of frozen water, kg m^{-2} s^{-1}
DKDT_DYN	Vertically integrated kinetic energy tendency for dynamics, W m^{-2}
DKDT_PHY	Vertically integrated kinetic energy tendency for physics, W m^{-2}
DKDT_ANA	Vertically integrated kinetic energy tendency for analysis, W m^{-2}
DHDT_DYN	Vertically integrated $c_P\ T_v$ tendency for dynamics, W m^{-2}
DHDT_PHY	Vertically integrated $c_P\ T_v$ tendency for physics, W m^{-2}
DHDT_ANA	Vertically integrated $c_P\ T_v$ tendency for analysis, W m^{-2}
DPDT_DYN	Potential energy tendency for dynamics, W m^{-2}
DPDT_PHY	Potential energy tendency for physics, W m^{-2}
DPDT_ANA	Potential energy tendency for analysis, W m^{-2}
CONVKE	Vertically integrated convergence of kinetic energy, W m^{-2}
CONVCPT	Vertically integrated convergence of virtual enthalpy, W m^{-2}
CONVPHI	Vertically integrated convergence of geopotential, W m^{-2}
SWTNT	TOA outgoing shortwave flux, W m^{-2}
SWGNT	Surface net downward shortwave flux, W m^{-2}
LWTUP	Upward TOA longwave flux, W m^{-2}
LWGNT	Net downward longwave flux at the surface, W m^{-2}
EFLUX	Latent heat flux (positive upward), W m^{-2}
HFLUX	Sensible heat flux (positive upward), W m^{-2}
PRECSN	Frozen precipitation at the surface, kg m^{-2} s^{-1}
DKDT_GEN	Generation of kinetic energy, W m^{-2}
TEFIXER	Total energy added by artificial energy "fixer," W m^{-2}

In the above definitions, "dynamics" refers to variable tendencies resulting from the hydrodynamics of the GEOS-5 dynamical core; "physics" refers to variable tendencies produced by the GEOS-5 physical parameterizations, which include moist processes, radiation, turbulent mixing, and surface processes; and "analysis" refers to tendencies resulting from the analysis increment, which is the difference between the observation-based analysis and the corresponding model synoptic background (Suarez 2011). A tendency may be expressed as the sum of these three components. For example, the tendency of vertically integrated water vapor (precipitable water) is expressed using MERRA variables as

$$\frac{\partial W_{(v)}}{\partial t} := \mathrm{DQVDT_DYN} + \mathrm{DQVDT_PHY} + \mathrm{DQVDT_ANA}. \quad \text{(A1)}$$

As described by Suarez (2011), monthly tendencies exactly match the difference of instantaneous values taken at the beginning and end of the averaging period.

Equation (2) is represented as

$$\frac{\partial A_E}{\partial t} := L_v(\mathrm{DQVDT_DYN} + \mathrm{DQVDT_PHY} + \mathrm{DQVDT_ANA}) - L_f(\mathrm{DQIDT_DYN} + \mathrm{DQIDT_PHY} + \mathrm{DQIDT_ANA}) + \mathrm{DHDT_DYN} + \mathrm{DHDT_PHY} + \mathrm{DHDT_ANA} + \mathrm{DPDT_DYN} + \mathrm{DPDT_PHY} + \mathrm{DPDT_ANA} + \mathrm{DKDT_DYN} + \mathrm{DKDT_PHY} + \mathrm{DKDT_ANA}. \quad \text{(A2)}$$

Equation (3) is represented as

$$\nabla \cdot \tilde{\mathbf{F}}_A := -(L_v\mathrm{DQVDT_DYN} - L_f\mathrm{DQIDT_DYN} + \mathrm{CONVKE} + \mathrm{CONVCPT} + \mathrm{CONVPHI}). \quad \text{(A3)}$$

Equations (4) and (A1) are represented as

$$R_{\mathrm{top}} + F_{\mathrm{sfc}} := (\mathrm{SWTNT} - \mathrm{LWTUP}) - (\mathrm{SWGNT} + \mathrm{LWGNT}) + \mathrm{EFLUX} + \mathrm{HFLUX} + L_f\mathrm{PRECSN}. \quad \text{(A4)}$$

The contribution of spurious residuals in the energy term is represented as

$$Q_{\mathrm{NUM}} := -\mathrm{DKDT_DYN} + \mathrm{CONVKE} + \mathrm{CONVPHI} + \mathrm{DKDT_GEN} - \mathrm{DPDT_DYN} - \mathrm{TEFIXER}. \quad \text{(A5)}$$

The remainder of Eq. (1) is given as

$$L_v\frac{\partial W_v}{\partial t}\bigg|_{\mathrm{CHM}} + \left(L_v\frac{\partial W_v}{\partial t} - L_f\frac{\partial W_i}{\partial t}\right)\bigg|_{\mathrm{FIL}} + \mathrm{ANA}_{(E)} := L_v\mathrm{DQVDT_CHM} + (L_v\mathrm{DQVDT_FIL} - L_f\mathrm{DQIDT_FIL}) + (L_v\mathrm{DQVDT_ANA} - L_f\mathrm{DQIDT_ANA} + \mathrm{DHDT_ANA} + \mathrm{DKDT_ANA} + \mathrm{DPDT_ANA}). \quad \text{(A6)}$$

REFERENCES

Barkstrom, B. R., 1984: The Earth Radiation Budget Experiment (ERBE). *Bull. Amer. Meteor. Soc.,* **65,** 1170–1185.

Bloom, S., L. Takacs, A. DaSilva, and D. Ledvina, 1996: Data assimilation using incremental analysis updates. *Mon. Wea. Rev.,* **124,** 1256–1271.

Bretherton, C. S., S. R. de Roode, C. Jakob, E. L Andreas, J. Intrieri, R. E. Moritz, and P. O. G. Persson, 2000: A comparison of the ECMWF forecast model with observations over the annual cycle at SHEBA. 46 pp. [Available online at http://citeseerx.ist.psu.edu/viewdoc/download?doi=10.1.1.36.9608&rep=rep1&type=pdf.]

Briegleb, B. P., and D. H. Bromwich, 1998: Polar climate simulations of the NCAR CCM3. *J. Climate,* **11,** 1270–1286.

Carroll, J. J., 1982: Long-term means and short-term variability of the surface energy balance components at South Pole. *J. Geophys. Res.,* **87,** 4277–4286.

Comiso, J. C., 2000: Variability and trends in Antarctic surface temperatures from in situ and satellite infrared measurements. *J. Climate,* **13,** 1674–1696.

Cullather, R. I., and M. G. Bosilovich, 2011: The moisture budget of the polar atmosphere in MERRA. *J. Climate,* **24,** 2861–2879.

Curry, J. A., J. L. Schramm, D. K. Perovich, and J. O. Pinto, 2001: Applications of SHEBA/FIRE data to evaluation of snow/ice albedo parameterizations. *J. Geophys. Res.,* **106,** 15 345–15 355.

Dee, D. P., 2005: Bias and data assimilation. *Quart. J. Roy. Meteor. Soc.,* **131,** 3323–3343.

Dorn, W., K. Dethloff, A. Rinke, S. Frickenhaus, R. Gerdes, M. Karcher, and F. Kauker, 2007: Sensitivities and uncertainties in a coupled regional atmosphere-ocean-ice model with respect to the simulation of Arctic sea ice. *J. Geophys. Res.,* **112,** D10118, doi:10.1029/2006JD007814.

Dutton, E. G., R. S. Stone, and J. J. DeLuisi, 1989: South Pole surface radiation balance measurements, April 1986 to February 1988. NOAA ERL Air Resources Laboratory Data Rep. Series 17, 49 pp.

Duynkerke, P., and S. de Roode, 2001: Surface energy balance and turbulence characteristics observed at the SHEBA Ice Camp during FIRE III. *J. Geophys. Res.,* **106,** 15 313–15 322.

Fasullo, J. T., and K. E. Trenberth, 2008: The annual cycle of the energy budget. Part I: Global mean and land–ocean exchanges. *J. Climate,* **21,** 2297–2312.

Francis, J. A., E. Hunter, and C.-Z. Zou, 2005: Arctic tropospheric winds derived from TOVS satellite retrievals. *J. Climate,* **18,** 2270–2285.

Genthon, C., and G. Krinner, 1998: Convergence and disposal of energy and moisture on the Antarctic polar cap from ECMWF reanalyses and forecasts. *J. Climate,* **11,** 1703–1716.

Gesch, D. B., 1994: Topographic data requirements for EOS global change research. Open-File Rep. 94-626, U.S. Geological Survey, 60 pp.

Gibson, J. K., P. Kållberg, S. Uppala, A. Hernandez, A. Nomura, and E. Serrano, 1997: ERA description. ECMWF Reanalysis Project Rep. Series 1, 72 pp.

Glickman, T. S., Ed., 2000: *Glossary of Meteorology*. 2nd ed. Amer. Meteor. Soc., 855 pp.

Gorodetskaya, I. V., and L.-B. Tremblay, 2008: Arctic cloud properties and radiative forcing from observations and their role in sea ice decline predicted by the NCAR CCSM3 model during the 21st century. *Arctic Sea Ice Decline: Observations, Projections, Mechanisms, and Implications, Geophys. Monogr.,* Vol. 180, Amer. Geophys. Union, 47–62.

Inoue, J., J. Liu, J. O. Pinto, and J. A. Curry, 2006: Intercomparison of Arctic regional climate models: Modeling clouds and radiation for SHEBA in May 1998. *J. Climate,* **19,** 4167–4178.

Josey, S. A., 2009: Southern Ocean air-sea flux climatologies and uncertainties. *Extended Abstracts, CLIVAR/CliC/SCAR Southern Ocean Region Implementation Panel Fifth Meeting,* Sydney, NSW, Australia, CLIVAR, World Climate Research Programme, 26 pp. [Available online at http://www.clivar.org/organization/southern/sop5_talks.php.]

Kalnay, E., and Coauthors, 1996: The NCEP/NCAR 40-Year Reanalysis Project. *Bull. Amer. Meteor. Soc.,* **77,** 437–472.

King, J. C., and J. Turner, 1997: *Antarctic Meteorology and Climatology*. Cambridge University Press, 409 pp.

Koster, R. D., M. J. Suárez, A. Ducharne, M. Stieglitz, and P. Kumar, 2000: A catchment-based approach to modeling land surface processes in a GCM. Part 1: Model structure. *J. Geophys. Res.,* **105,** 24 809–24 822.

Langland, R. H., R. N. Maue, and C. H. Bishop, 2008: Uncertainty in atmospheric temperature analyses. *Tellus,* **60A,** 598–603.

Levitus, S., 1984: Annual cycle of temperature and heat storage in the world ocean. *J. Phys. Oceanogr.,* **14,** 727–746.

Lin, B., P. Minnis, A. Fan, J. A. Curry, and H. Gerber, 2001: Comparison of cloud liquid water paths derived from in situ and microwave radiometer data taken during the SHEBA/FIREACE. *Geophys. Res. Lett.,* **28,** 975–978.

Loeb, N. G., B. A. Wielicki, D. R. Doelling, G. L. Smith, D. F. Keyes, S. Kato, N. Manalo-Smith, and T. Wong, 2009: Toward optimal closure of the Earth's top-of-atmosphere radiation budget. *J. Climate,* **22,** 748–766.

Moody, E. G., M. D. King, S. Platnick, C. B. Schaaf, and F. Gao, 2005: Spatially complete global spectral surface albedos: Value-added datasets derived from Terra MODIS land products. *IEEE Trans. Geosci. Remote Sens.,* **43,** 144–158.

Moore, J. K., M. R. Abbott, and J. G. Richman, 1999: Location and dynamics of the Antarctic Polar Front from satellite sea surface temperature data. *J. Geophys. Res.,* **104,** 3059–3073.

Nakamura, N., and A. H. Oort, 1988: Atmospheric heat budgets of the polar regions. *J. Geophys. Res.,* **93,** 9510–9524.

Ohata, T., N. Ishikawa, S. Kobayashi, and S. Kawaguchi, 1985: Heat balance at the snow surface in a katabatic wind zone, East Antarctica. *Ann. Glaciol.,* **6,** 174–177.

Okada, I., and T. Yamanouchi, 2002: Seasonal change of the atmospheric heat budget over the Southern Ocean from ECMWF and ERBE data. *J. Climate,* **15,** 2527–2536.

Onogi, K., and Coauthors, 2007: The JRA-25 Reanalysis. *J. Meteor. Soc. Japan,* **85,** 369–432.

Oort, A. H., 1983: Global atmospheric circulation statistics, 1958-1973. NOAA Professional Paper 14, 180 pp. and 47 microfiche.

Perovich, D. K., T. C. Grenfell, J. A. Richter-Menge, B. Light, W. B. Tucker III, and H. Eicken, 2003: Thin and thinner: Sea ice mass balance measurements during SHEBA. *J. Geophys. Res.,* **108,** 8050, doi:10.1029/2001JC001079.

Porter, D. F., J. J. Cassano, M. C. Serreze, and D. N. Kindig, 2010: New estimates of the large-scale Arctic atmosphere energy budget. *J. Geophys. Res.,* **115,** D08108, doi:10.1029/2009JD012653.

Randall, D., and Coauthors, 1998: Status of and outlook for large-scale modeling of atmosphere–ice–ocean interactions in the Arctic. *Bull. Amer. Meteor. Soc.,* **79,** 197–219.

Reichle, R. H., R. D. Koster, G. J. M. De Lannoy, B. A. Forman, Q. Liu, S. P. P. Mahanama, and A. Touré, 2011: Assessment and enhancement of MERRA land surface hydrology estimates. *J. Climate,* **24,** 6322–6338.

Reijmer, C. H., and J. Oerlemans, 2002: Temporal and spatial variability of the surface energy balance in Dronning Maud Land, East Antarctica. *J. Geophys. Res.,* **107,** 4759, doi:10.1029/2000JD000110.

Reynolds, R. W., N. A. Rayner, T. M. Smith, D. C. Stokes, and W. Wang, 2002: An improved in situ and satellite SST analysis for climate. *J. Climate,* **15,** 1609–1625.

Rienecker, M. M., and Coauthors, 2008: The GEOS-5 Data Assimilation System—Documentation of Versions 5.0.1, 5.1.0, and 5.2.0. Tech. Rep. Series on Global Modeling and Data Assimilation, M. J. Suarez, Ed., NASA/TM-2008-104606, Vol. 27, National Aeronautics and Space Administration Goddard Space Flight Center, 95 pp.

——, and Coauthors, 2011: MERRA–NASA's Modern-Era Retrospective Analysis for Research and Applications. *J. Climate,* **24,** 3624–3648.

Saha, S., and Coauthors, 2010: The NCEP Climate Forecast System Reanalysis. *Bull. Amer. Meteor. Soc.,* **91,** 1015–1057.

Sedlacek, J., J.-F. Lemieux, L. A. Mysak, L. B. Tremblay, and D. M. Holland, 2007: The granular sea ice model in spherical coordinates and its application to a global climate model. *J. Climate,* **20,** 5946–5961.

Serreze, M. C., A. P. Barrett, A. G. Slater, M. Steele, J. Zhang, and K. E. Trenberth, 2007: The large-scale energy budget of the Arctic. *J. Geophys. Res.,* **112,** D11122, doi:10.1029/2006JD008230.

Simmons, A. J., S. Uppala, D. Dee, and S. Kobayashi, 2007: ERA-Interim: New ECMWF reanalysis products from 1989 onwards. *ECMWF Newsletter,* No. 110, ECMWF, Reading, United Kingdom, 25–35.

Sorteberg, A., and J. E. Walsh, 2008: Seasonal cyclone variability at 70°N and its impact on moisture transport into the Arctic. *Tellus,* **60A,** 570–586.

——, V. Kattsov, J. E. Walsh, and T. Pavlova, 2007: The Arctic surface energy budget as simulated with the IPCC AR4 AOGCMs. *Climate Dyn.,* **29,** 131–156.

Stieglitz, M., A. Ducharne, R. D. Koster, and M. J. Suarez, 2001: The impact of detailed snow physics on the simulation of snow cover and subsurface thermodynamics at continental scales. *J. Hydrometeor.,* **2,** 228–242.

Suarez, M., 2011: File specification for MERRA products. NASA Tech. Memo., 90 pp. [Available from Global Modeling and Assimilation Office, Earth Sciences Division, NASA Goddard Space Flight Center, NASA/GSFC Code 610.1, 8800 Greenbelt Road, Greenbelt, MD 20771.]

Trenberth, K. E., 1997: Using atmospheric budgets as a constraint on surface fluxes. *J. Climate,* **10,** 2796–2809.

——, J. T. Fasullo, and J. Kiehl, 2009: Earth's global energy budget. *Bull. Amer. Meteor. Soc.,* **90,** 311–323.

Uppala, S. M., and Coauthors, 2005: The ERA-40 Re-Analysis. *Quart. J. Roy. Meteor. Soc.,* **131,** 2961–3012.

Uttal, T., and Coauthors, 2002: Surface heat budget of the Arctic Ocean. *Bull. Amer. Meteor. Soc.,* **83,** 255–275.

Wielicki, B. A., B. R. Barkstrom, E. F. Harrison, R. B. Lee, G. L. Smith, and J. E. Cooper, 1996: Clouds and the Earth's Radiant Energy System (CERES): An Earth Observing System experiment. *Bull. Amer. Meteor. Soc.,* **77,** 853–868.